Nanoscale Advances

ROYAL SOCIETY OF CHEMISTRY

PAPER

View Article Online
View Journal | View Issue

Cite this: *Nanoscale Adv.*, 2025, **7**, 2686

Polarity-sensitive dual emissive fluorescent carbon dots as highly specific targeting probes for lipid droplets in live cells†

Aminakutty Neerkattil, ‡[a] M. M. Bijeesh,‡[b] K. K. Ghosh,[c] Parasuraman Padmanabhan, [cd] Balázs Gulyás,[cd] V. M. Murukeshan*[b] and Jayeeta Bhattacharyya*[a]

Polarity-sensitive fluorescent nanoparticles with intrinsic dual emission are invaluable tools for investigating microenvironmental polarity. Ratiometric fluorescent sensors, with their built-in self-calibration characteristics, offer higher sensitivity and more obvious visual detection in qualitative and quantitative analysis. In this context, we report the synthesis of polarity-sensitive, dual-emitting carbon dots *via* a solvothermal method and demonstrate their application in ratiometric polarity sensing. These carbon dots exhibit characteristic solvatochromic effects with emissions in both the blue and red spectral regions. Notably, we observed a remarkable 30-fold enhancement in the red-to-blue emission intensity ratio as the solvent polarity shifted from 0.245 to 0.318. The dual-emitting carbon dots demonstrate the highly sensitive and inherently reliable (self-calibration) polarity dependence of the emission spectra, facilitating their application in ratiometric polarity sensing. These dual-emitting carbon dots exhibited a strong affinity for lipid droplets in live cells, demonstrating their potential as highly specific targeting probes for imaging lipid droplets in live cells, without the need for additional targeting ligands. The characteristics of excellent biocompatibility, photostability, and good cellular imaging capabilities make these dual-emitting carbon dots highly promising for biomedical and sensing applications.

Received 15th January 2025
Accepted 14th March 2025

DOI: 10.1039/d5na00061k

rsc.li/nanoscale-advances

1. Introduction

Fluorescence imaging is an important technique for understanding the structural and physiological functions of cells and organisms, playing a crucial role in biomedical research and the diagnosis of several diseases.[1] Among various cellular components and biological processes, lipid droplets (LDs) have attracted particular attention from researchers due to their essential roles in metabolism and disease pathology. LDs were initially assumed to be reservoirs for storing excess lipids in cells. However, they were later identified as essential organelles that regulate membrane and lipoprotein formation and play a vital role in intracellular signal transduction in live cells.[2,3] LDs are composed of triacylglycerol and cholesteryl esters.[4] Recently, it was found that there is a correlation between nuclear morphology and cytoplasmic LD formation.[5] The energy stored in lipids is released by the biogenesis of LDs and is used for various cell bioprocesses.[2,6] The synthesis of lipids, nucleation, and their cytoplasmic budding are the multiple steps in forming LDs in live cells. The dysregulation or excessive formation of LDs will lead to numerous diseases, such as fatty liver, obesity, diabetes, Alzheimer's, dementia, cardiovascular diseases, *etc.*[6,7] The association of LDs leading to various forms of cancer is still not well understood.[5,8] Understanding the disease pathways related to lipids is crucial in treatments, especially under pathogenic conditions.[3,9]

Several fluorescent probes targeting LDs have been reported based on small fluorescent organic molecules, fluorescent nanoparticles, and fluorescent proteins.[10,11] Various commercially available dyes have also been used to detect and image LDs, including Nile red, oil red, BODIPY 498/503, and LipidSpot 498/633.[12] These dyes suffer from a small Stokes shift and some of them can only be used in fixed cells, and they have weak specificity due to nonspecific binding to lipophilic sites other than LDs in a cell, restricting their proper application at the cellular level and hence failing to identify tissue microstructures.[3,4,9] Therefore, it is necessary to develop new LD fluorescent probes with simple preparation, large Stokes shift, and high LD staining selectivity.

[a]*Department of Physics, Indian Institute of Technology Madras, Chennai, Tamil Nadu, India. E-mail: jayeeta@iitm.ac.in*

[b]*Centre for Optical and Laser Engineering (COLE), School of Mechanical and Aerospace Engineering, Nanyang Technological University, Singapore. E-mail: mmurukeshan@ntu.edu.sg*

[c]*Lee Kong Chian School of Medicine, Nanyang Technological University, Singapore*

[d]*Cognitive Neuroimaging Centre, Nanyang Technological University, Singapore*

† Electronic supplementary information (ESI) available. See DOI: https://doi.org/10.1039/d5na00061k

‡ These authors contributed equally to this work.

Carbon dots (CDs) are a new type of carbon-based nanomaterial and have attracted significant research interest over the years.[13] CDs are fluorescent nanoparticles composed of a carbon core and surface structure having functional groups such as amine, carboxyl, hydroxyl, *etc.* Due to their non-toxicity, high fluorescence emission quantum yield, photostability, and good biocompatibility, they are promising candidates for bioimaging and sensors.[1,14,15] The emission properties of CDs primarily depend on the surface states.[16] Thus, the tunability of emission wavelengths, efficiency, and selectivity can be obtained by optimizing the precursors and dopants used during synthesis, as well as the surrounding media in which the CDs are dispersed.[17,18] Thus, CDs show great potential for bioimaging and sensing by modifying surface structures.[19,20] CD-based fluorescence imaging methods are gaining significant attention due to their excellent water solubility, biocompatibility, and unique optical properties.[14,15] Researchers have developed various CD fluorescent probes for lipid droplet imaging,[3] tracking LD catabolism,[21] imaging the lipid-rich tissues of zebrafish,[22] and simultaneous dual labeling of LDs and lysosomes.[23] However, most of these previously reported fluorescent probes suffer from some inherent limitations, such as short emission wavelengths, less selectivity towards LDs, and poor photostability.[24] Besides, in some cases, a relatively high working concentration of the probes is required to obtain the desired imaging performance.[24]

Dual emitting carbon dots (DCDs) offer superior quantification capabilities compared to single-emitting CDs, but most reported DCDs primarily emit blue or green fluorescence at their effective excitation wavelengths.[25] These emissions can interfere with cellular autofluorescence, complicating bioimaging applications. Polarity-sensitive fluorescent probes are powerful tools for studying the structures and functions of biomolecules, both *in vitro* and *in vivo*.[26] LDs, rich in triglycerides and sterol esters, are cellular organelles that store and produce energy with very low water content and extremely low polarity.[27] Therefore, there is an urgent need to develop a polarity-sensitive fluorescent probe for targeting lipid droplets (LDs) that is highly specific, emits at longer wavelengths, offers high photostability, and ensures good cell viability.

Polarity is an integral microenvironment parameter. Several fluorescent probes in response to polarity have gradually emerged. Meanwhile, CDs with good surface functionalization can show a sensitive fluorescence response to external stimuli, which is desirable for sensing. However, sensing and quantification methods currently used depend on fluorescent enhancement or quenching at a single wavelength, making quantification challenging due to various parameters, such as instrumental calibration, local target concentration, microenvironment, photobleaching, *etc*.[25] A ratiometric assay is one of the most effective solutions to this problem, and the quantification process relies on target-induced changes from at least two emission bands, which provide an effective internal reference to increase sensitivity, stability, and accuracy.[28] CD-based ratiometric fluorescence probes can be synthesized through physical mixing,[20,29] nanohybrid formation,[25] or direct synthesis of DCDs, with the latter offering a simpler and more accurate approach by inherently providing dual emissions without the need for additional optical materials.[30] Researchers have synthesized DCDs using various precursors and methods, including environmentally friendly approaches using biomass materials, enabling their applications in the ratiometric detection of heavy metal ions, 2,4,6-trinitrophenol (TNP), copper (Cu), glutathione (GSH), veterinary drug residues, chromium (Cr), intracellular lysine, pH sensing, and cell imaging.[30–35] The reported synthesis and ratiometric fluorescence sensing applications of DCDs are presented in Table 1. Although these previous studies have realized different ratiometric sensing applications of DCDs, the ratiometric fluorescence polarity sensing of DCDs has not been reported.

Table 1 A summary of DCD-based ratiometric fluorescence probes

Synthesis method	Emission properties	Applications	Reference
Hydrothermal carbonization method	440 nm and 624 nm	Ratiometric detection of intracellular lysine and pH	31
Hydrothermal method	468 nm and 628 nm	Ratiometric fluorescence detection of Cr and application in cellular imaging	32
Hydrothermal method	595 nm and 648 nm	pH sensor, Ag^{+} detection, and cell imaging	33
Hydrothermal method	597 nm and 645 nm	Ratiometric sensing of veterinary drugs	34
Solvothermal reaction	430 nm and 550 nm	Ratiometric fluorescent sensor for the analysis of TNP and visualizing intracellular TNP in live HeLa cells	35
Microwave-assisted heat treatment	360 nm and 530 nm	Ratiometric fluorescent sensor for Cu^{2+}	30
Hydrothermal method	430 nm and 642 nm	Ratiometric glutathione (GSH) sensing and differentiating cancer cells from normal cells	36
Hydrothermal method	630 nm and 680 nm	Ratiometric fluorescent sensor for methyl blue, pH and cell imaging	37

In this work, we developed polarity-sensitive DCDs, which worked as a ratiometric sensor for polarity and were used for imaging LDs in HeLa cells without further modification. We systematically analysed the DCDs and showed that they primarily comprise a carbonized core with various functional groups on its surface, contributing to their remarkable optical properties. The DCDs have characteristic solvatochromic effects and display dual emissions in the blue and red spectral regions, showing low toxicity and good photostability. We demonstrated an approximately 30-fold enhancement in the intensity ratio of red to blue emissions of DCDs when the solvent polarity (Δf) was changed from 0.245 to 0.318, allowing the detection of very small polarity changes. This property of DCDs facilitates the application of the DCDs as promising ratiometric fluorescent polarity sensors. Subsequently, the photoluminescence (PL) properties of DCDs in the DI water–silicone oil system were studied to understand the PL mechanism of DCDs towards lipids. DCDs emit bright blue fluorescence in DI water, whereas the PL intensity of red emission is enhanced in the vicinity of lipids in an aqueous solution. This suggests that DCDs exhibit higher PL efficiency at red wavelengths in lower polarity environments. These findings indicate the potential application of DCDs for imaging LDs in live cells, as LDs are known to have lower polarity compared to the cytoplasm. This was further confirmed by imaging LDs in HeLa cells. These studies and results suggest that DCDs could serve as highly specific targeting probes for LDs, with promising applications in biomedical research, clinical diagnostics, and ratiometric polarity sensing.

2. Results and discussion

2.1 Synthesis and structural properties of DCDs

The DCDs were synthesized by the solvothermal method. Formamide was utilized as the reaction solvent and nitrogen dopant, anhydrous citric acid (CA) served as a carbon source, tris(hydroxymethyl) amino methane (tris buffer) was used as an electron-donating source, and polyethylene glycol (PEG400) was selected as a surface coating agent.[38] The detailed synthesis method is given in experimental section 3.2. To investigate the microstructure of the synthesized DCDs, high-resolution transmission electron microscopy (HR-TEM), X-ray diffraction (XRD), and Raman spectroscopy were employed.

The XRD patterns of the DCDs are shown in Fig. 1(a). Most reported CDs show a broad XRD pattern[39] between 20° and 40°. The diffraction peak at $2\theta = 26.8°$ shown in the XRD pattern is identified as the (002) plane of graphite.[23] This peak corresponds to an interlayer spacing of 0.32 nm, which is very close to the interlayer stacking of 0.334 nm in graphite.[40] Thus, from the XRD peak position and width, we can conclude that the DCDs consisted of a graphitic core with good crystallinity. The Raman spectrum of the DCDs (Fig. 1(b)) shows two distinctive peaks at about 1343 cm^{-1} for the D-band and 1570 cm^{-1} for the G-band, which are assigned to sp^3 and sp^2 hybridized carbon atoms, respectively.[41] The peaks in Raman spectra imply the existence of a graphitic carbon core with sp^3 carbon defects either on the surface or within the core.[39] The ratio of intensities of the D and G peaks is about 1.05, suggesting that the DCDs contain a significant number of nitrogen atoms incorporated as defects, within the sp^2 framework.[38]

The HR-TEM image (Fig. 2(a)) shows the successful formation of DCDs. It is also observed that the dots are well separated and do not form aggregates. The size distribution histogram (Fig. 2(b)), obtained from about 100 dots, indicates an average size of 7 ± 2 nm. Well-separated small dots of a few nm are essential for penetrating into the cell membrane to enable fluorescence imaging within the cell. The inset of Fig. 2(a), captured at a higher resolution, exhibits well-resolved lattice fringes in the DCDs, with a lattice spacing of 0.32 nm, corresponding to the (002) in-plane lattice of graphene carbons. This indicates some degree of crystallinity of the grown DCDs.[23]

As stated earlier, the optical properties of CDs, in general, are dominated by the functional groups attached to the surface of the dots or incorporated within. We used Fourier transform infrared (FTIR) spectroscopy to identify the surface functional groups of the DCDs. The FTIR spectrum of the DCDs (Fig. 3(a)) shows distinctive peaks at 2915 cm^{-1} and 2850 cm^{-1}, indicating the presence of methyl groups (CH_3).[23] The stretching vibrations of $-NH_2$ and aromatic C–NH can be observed at 3170 cm^{-1} and 1211 cm^{-1}, respectively, while the peaks observed at 1550 cm^{-1}–1750 cm^{-1} are ascribed to the stretching vibrations of C=O/C=N and the bending vibration of $-NH_2$.[42] Additionally, peaks around 1548 cm^{-1}–1334 cm^{-1}

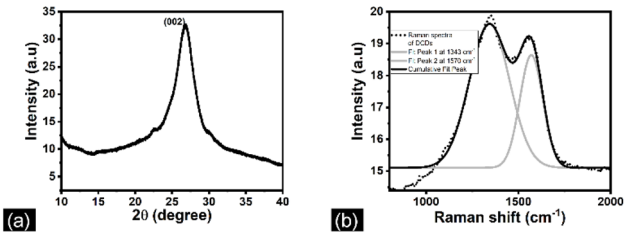

Fig. 1 (a) The XRD profile of DCDs. The XRD spectrum shows the peak at $2\theta = 26°$, corresponding to the (002) plane of graphite. (b) Raman spectra of the DCDs. The dotted line represents the measured Raman spectrum of the DCDs. The solid black line is the fit to the data, consisting of two Gaussian curves (grey lines) with peaks at about 1343 cm^{-1} for the D-band and 1570 cm^{-1} for the G-band.

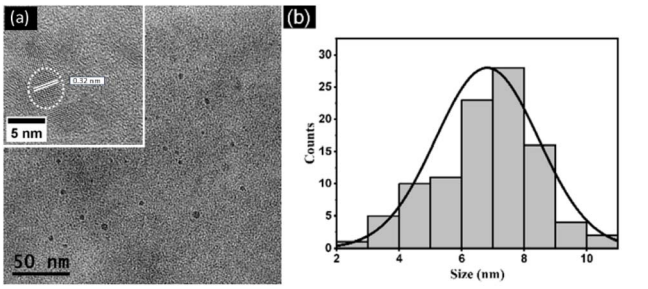

Fig. 2 (a) HR-TEM image of DCDs showing well-dispersed nanoparticles with the inset image depicting well-resolved lattice fringes. (b) Size distribution histogram of DCDs indicating an average size of 7 ± 2 nm.

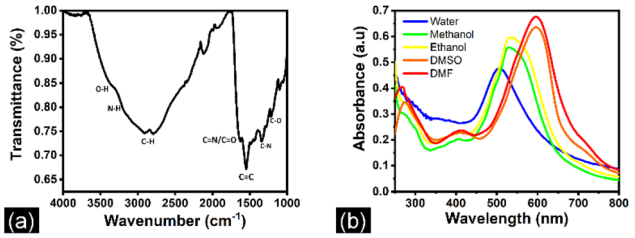

Fig. 3 (a) FTIR spectrum of DCDs. Several different frequencies were seen in the FTIR spectrum, corresponding to the various stretching and bonding vibrations of different functional groups. (b) UV–vis absorption spectra of DCDs. The absorption spectrum shows a broad absorption across the visible region, with a significant peak between 500 and 600 nm.

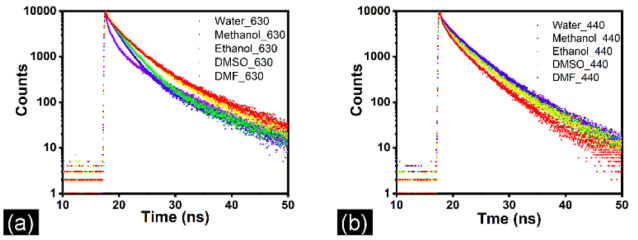

Fig. 4 PL decay of CDs in various solvents (a) at 630 nm and (b) at 440 nm under 405 nm excitation.

correspond to the C=C backbone of the benzene ring and the stretching vibrations of C–N=.[43]

2.2 Optical properties of DCDs

Ultraviolet–visible (UV) absorption, PL spectroscopy, and lifetime decay were used to investigate the optical characteristics of DCDs. The absorption spectra of DCDs at a concentration of 10 μg mL^{-1}, dispersed in various solvents (deionized (DI) water, methanol, ethanol, dimethyl sulfoxide (DMSO), and *N*,*N*-dimethyl formamide (DMF)), are presented in Fig. 3(b). These spectra demonstrate a gradual shift as the solvent polarity changes from polar protic (DI water, methanol, and ethanol) to aprotic (DMSO and DMF) solvents. The DCDs are insoluble in aprotic nonpolar solvents such as chloroform, toluene, and cyclohexane, preventing the measurement of their optical properties in these solvents. The maximum absorption wavelength of the DCDs depends on the polarity of the solvents. The absorption spectrum shows a broad absorption across the visible region, with a significant peak between 500 nm and 600 nm. In methanol and ethanol, the absorption spectra become more intense and shift to longer wavelengths, moving from 505 nm to 530 nm compared to DI water, while another peak at 410 nm is still visible (Fig. 3(b)). In DMSO, the absorption intensity increases further compared to that of ethanol, with the main peak red-shifted to 595 nm and the peak emerging at 410 nm remaining the same, accompanied by a shoulder peak at 280 nm. The peak at 280 nm is attributed to π–π* transitions within the sp^2 hybridized carbon–carbon (C=C) bonds present in the graphitic core of the DCDs. The peak at 410 nm and the significant peak between 500 nm and 600 nm are associated with the π–π* and n–π* transitions of the aromatic π system containing many C–N/C=N or C–O/C=O structures on the surface of the DCDs.[44,45] The absorption spectrum of CDs in DMSO closely resembles that of DCDs in DMF (Fig. 3(b)).

Fig. 4(a) and (b) display the PL decays of DCDs in various solvents, monitored at 630 nm and 440 nm under 405 nm laser excitation. The average PL lifetimes, calculated using bi-exponential and tri-exponential fits, show an increase for the 630 nm emission and a slight decrease for the 440 nm emission as the solvent changes from DI water to methanol, ethanol, DMSO, and DMF. At 440 nm emission, the average PL lifetime in DI water is 3.63 ns. In methanol and ethanol, the PL lifetime decreases to 3.53 ns and 3.32 ns, respectively. In DMSO and DMF, the PL lifetime of DCDs decreases further to 3.12 ns and 2.58 ns, respectively. At 630 nm emission, the average PL lifetime increases to 2.32 ns, 2.48 ns, and 2.82 ns as the solvent changes from DI water, methanol, and ethanol, respectively. In DMSO and DMF, the PL lifetime of DCDs extends further to 3.53 ns and 3.76 ns, respectively. It is reported that changes in solvent polarity typically cause a shift in the excited state energy through interactions between solvent dipoles and the fluorophore in the excited state, leading to further relaxation.[46] This usually manifests as a red shift in the PL spectra with increasing solvent polarity.[47] Several studies have reported distinct lifetimes in CDs, though their origins remain debated. Liu *et al.* attributed the fast component (~1.32 ns) to radiative recombination from intrinsic states and the slower component (~7.89 ns) to emissions from defect states.[48] In contrast, Zhao *et al.* associated the fast lifetimes (1.29–1.73 ns) with radiative recombination of eigenstates and the slower ones (2.51–7.16 ns) with non-radiative processes involving surface defects.[49] Byun's group proposed that the fast lifetimes (1.17–3.15 ns) arise from non-radiative recombination, while the slower ones (5.7–8.52 ns) result from radiative recombination of oxygen-induced defects.[50] From the transient measurements, we can conclude that the origin of the blue emission, which has less dependency on the polarity of the solvent, may arise from the core/edge state, and the red emission, which largely depends on the solvent polarity, may arise from the surface states.

The PL spectra of DCDs dispersed in DI water are shown in ESI.† The photoluminescence excitation (PLE) spectrum (Fig. S1†) indicated that 394 nm is the optimum excitation wavelength for the maximum emission of DCDs in DI water. Their excitation-dependent nature was investigated to gain an

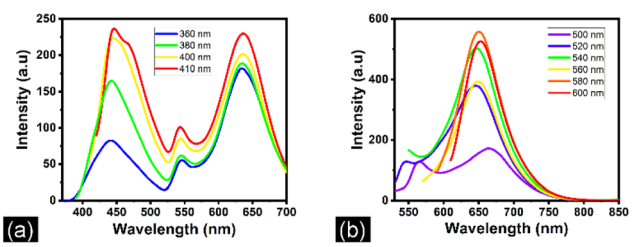

Fig. 5 PL emission spectra of DCDs (a) and (b) in DMSO solution at different excitation wavelengths.

additional understanding of the emission properties of DCDs. The DCDs clearly show an excitation-dependent emission. The excitation dependence of PL for DCDs is more evident from Fig. 5(a) and (b), which depict the PL of DCDs dispersed in DMSO for different excitation wavelengths. The PL spectra of DCDs in DMSO show two distinct emission peaks, one at 440 nm and one at 630 nm; both are independent of the excitation wavelength. In contrast to emission from DCDs in DI water, the emission intensity of the peak at 630 nm increased with an increase in the excitation wavelength.

2.3 Polarity sensing of DCDs

The PL spectra of DCDs dispersed in different polarity solvents are shown in Fig. 6(a). As the solvent changes from DI water to ethanol, the PL peak intensity at 440 nm decreases, and the peak intensity at 630 nm increases, with additional narrow peaks appearing at 540 nm. Further changes to DMSO and DMF result in a continued increase in PL intensity and a shift of the PL peaks to 630 nm. Fig. 6(b) shows the images of DCDs dissolved in various solvents under daylight and UV irradiation. The emission from DCDs changes from red to blue as the solvent varies from DMF to DI water under 360 nm UV light excitation.

To further investigate the polarity sensitivity of DCDs, a series of linearly varying polarity solvents were prepared by mixing DI water and DMSO at different concentrations. The Lippert–Mataga polarity (Δf) parameter was utilized to define the polarity of the solvents.[51] The concentration of DMSO was changed from 0 to 100 percent, creating a polarity change (Δf) from 0.3274 to 0.2230. The PL spectra of DCDs, at 360 nm excitation, for different concentrations of DMSO in DI water are shown in Fig. 7(a). With increasing DMSO concentration, from 0 to 100%, the intensity of the blue emission decreases by a factor of about 3, and the intensity of the red emission increases by a factor of about 30. Thus, both the blue and the red emissions are sensitive to the polarity of the solvents. A 30-fold systematic change in fluorescence intensity for the red emission with a polarity change from 0.3274 to 0.2230 is a highly desirable criterion for a fluorescence-based polarity sensor. The ratio of the intensities of the emission peaks at 630 nm and 440 nm as a function of the concentration of DMSO is shown in Fig. 7(b). The plot demonstrates a linear

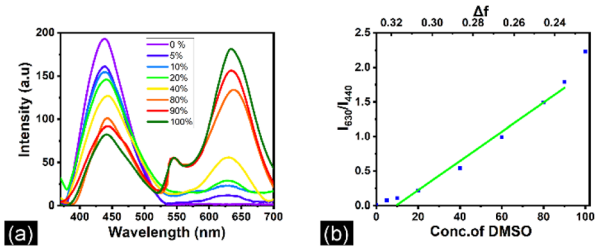

Fig. 7 PL titration of DCDs (a) with different concentrations of DMSO/DI water under 360 nm excitation. With increasing DMSO concentration, the intensity of the blue emission decreases by a factor of about 3, and the intensity of the red emission increases by a factor of about 30. (b) The ratio of intensities *vs.* concentration of the DMSO plot. The plot shows a linear relationship between the concentration of DMSO in DI water and the intensity ratio. The ratio of intensities *vs.* polarity change plot. The plot shows a linear relationship between the polarity change (Δf from 0.235 to 0.318) and the ratio of the red and blue peak intensities. Different micro-polarity values in solution (Δf = 0.2230–0.3274) were obtained by mixing DI water and DMSO solutions.

dependence (R^2 = 0.99) between the concentration of DMSO (with Δf ranging from 0.3274 to 0.2230) and the intensity ratio of the emission peaks. The linear relationship between the emission ratiometric signal I_{630}/I_{440} and the polarity change allows the detection of very small polarity changes through the fluorescent ratiometric signal. This suggests that DCDs can function as ratiometric fluorescence sensors for polarity, offering advantages over traditional sensors by being less sensitive to environmental interference and providing self-calibration.

The polarity response of the DCDs was further verified in a different polarity system comprising ethanol and DI water. DCDs demonstrated a polarity-sensitive ratiometric fluorescence emission behavior in the mixture, as presented in the ESI (Fig. S4†). The effect of pH on the PL properties of DCDs is also investigated by varying pH from 4 to 11 under 360 nm excitation (Fig. S3†). Given that DCDs exhibit polarity-dependent emission, we further explored a DI water–silicone system to investigate lipid detection in aqueous media, intending to image lipid droplets in a cellular environment. To achieve this, we mixed silicone oil, DI water, and DCDs in a vortex mixer, and oil droplets were formed. This gives a system of lipid-rich regions in aqueous media. Subsequently, the PL in different regions was

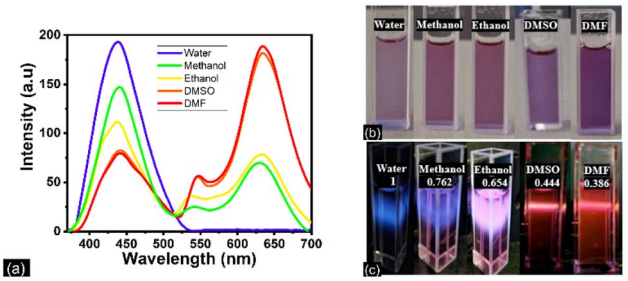

Fig. 6 (a) PL emission spectra of DCDs in various solvents for an excitation wavelength of 360 nm. Photograph of DCDs dissolved in various solvents (b) under daylight and (c) under UV irradiation.

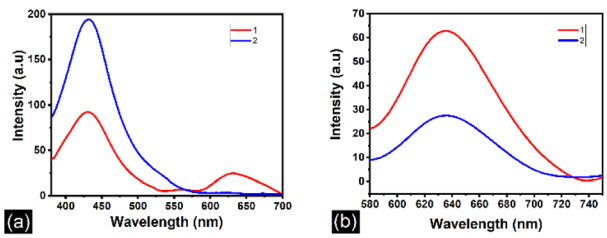

Fig. 8 PL emission spectra of DCDs in DI water–LD solution at (a) 360 nm and (b) 560 nm excitation wavelengths. 1 represents emission taken from DCDs in DI water, and 2 represents emission taken from the lipid-rich region.

measured, where DCDs showed good PL with the optimal PL excitation wavelength located at around 360 nm for lipids in DI water (Fig. 8). Moreover, DCDs emit bright blue fluorescence in DI water, whereas red emission is enhanced in the vicinity of lipid-rich regions in aqueous solution, which indicates the higher PL efficiency of the dots at red wavelengths towards lower polarity regions. Also, the PL intensity of red emission is enhanced at an excitation wavelength of 560 nm, as shown in Fig. 8(b). This indicates that the PL intensity enhancement of DCDs in the lower polarity regions provides an opportunity for imaging LDs in live cells since the LDs exhibit lower polarity than the cytoplasm.

2.4 Bioimaging and LD targeted staining by DCDs

To explore the application of DCDs in live cell imaging, the cytotoxicity of the DCDs was studied by using an MTT assay. We found that DCD concentrations up to 100 μg mL^{-1} were safe to use, with approximately 83% viable cells (Fig. 9(e)). This indicates the low cytotoxicity of the probe DCDs, which can be used for fluorescence imaging without further modification. The dominant emission of the DCDs falls in the red spectral regime, which is away from auto-fluorescence, indicating potential applications in bioimaging. We, therefore, investigated the use of DCDs as a fluorescent probe for biomolecular imaging. The bioimaging capability of the DCDs was studied by labeling HeLa cells with DCDs. The confocal images of HeLa cells labeled with a 50 μg mL^{-1} concentration of DCDs under 560 nm excitation are shown in the ESI (Fig. S5†). The images show a bright fluorescent signal in the cytoplasm and relatively lower emission from the nucleus, demonstrating the excellent cellular imaging capabilities of the synthesized DCDs.

Since the DCDs exhibit considerable polarity-dependent fluorescence emission, we have examined their potential application in imaging LDs in live cells. The LDs were induced in HeLa cells by adding oleic acid (OA) to the cells and then labeled with DCDs. After OA treatment, confocal microscopy should show vesicle-like droplets in the cytoplasm. Fig. 9(a)–(d) show the images of HeLa cells treated with OA and DCDs. The fluorescent areas in the HeLa cells were identified as LDs (Fig. 9(b)) from colocalization images obtained using a commercial lipid probe. The LipidSpot dye targets the LDs and emits green fluorescence upon excitation with a 488 nm laser (Fig. 9(a)). The bright field image identifies the cell boundaries (Fig. 9(c)). As illustrated in Fig. 9(d), the merged confocal laser scanning microscope (CLSM) images distinctly demonstrate the effective colocalization of DCDs with LipidSpot 488 dye. Moreover, Pearson's correlation coefficient was determined to be 0.91 (Fig. S9†) for the images, which confirms the ability of DCDs to specifically stain LDs. A more in-depth comparison with existing lipid droplet probes, such as Nile Red or BODIPY dyes, is given in ESI (Table S1†) to highlight the advantages of DCDs in terms of specificity, photostability, biocompatibility, and signal-to-noise ratio. The depth-dependent localization of DCDs in lipid droplets (LDs) was further investigated by imaging cells at varying depths using the Z-sectioning capability of the confocal microscope. The 3D projection (ESI†) generated from the confocal sections reveals that the DCDs are localized in a three-dimensional configuration within the cells (Fig. S8†). Further, cells treated with only OA are used for control experiments (Fig. S7†) to show that no fluorescence is emitted from the cells or LDs under laser excitation.

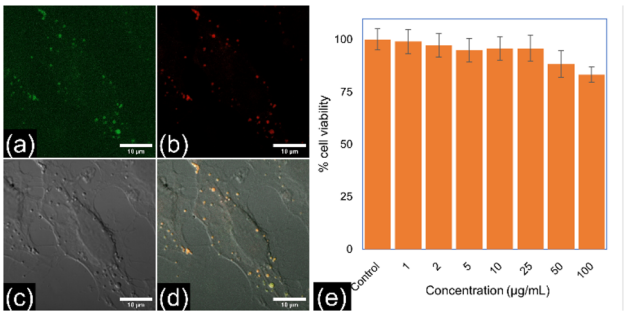

Fig. 9 (a–d) CLSM images of lipid droplet co-localization of DCDs (5 μg mL^{-1}) and LipidSpot 488 dye in HeLa cells. (a) LipidSpot 488 dye, (b) DCDs, (c) bright-field image of HeLa cells and (d) merged image of (a) and (b). The merged CLSM images distinctly demonstrate the effective colocalization of DCDs with LipidSpot 488 dye, which confirms the specific ability of DCDs to stain LDs. (e) Cell viability of HeLa cells after incubation with various DCD concentrations.

2.5 Anti-interference and photostability studies of DCDs

Fluorescent probes must be highly resistant to interference. To explore the anti-interference ability of the DCDs, we added different analytes to the test solution to detect changes in the fluorescence spectrum. As shown in Fig. 10, the fluorescence spectra were collected at 360 nm excitation, and the emission was measured at 440 nm by adding different analytes to DCDs dissolved in DI water. The results showed the change in fluorescence intensity and peak shift was almost negligible, and DCDs possessed favourable anti-interference ability with excellent selectivity towards polarity.

The photostability of the probe is assessed by measuring the PL intensity of DCDs under continuous UV irradiation for different time intervals. The PL intensity for different time intervals under continuous UV (360 nm) excitation is shown in the ESI (Fig. S6†). The fluorescence intensity of the DCDs in DMSO was nearly constant even after being exposed to 360 nm

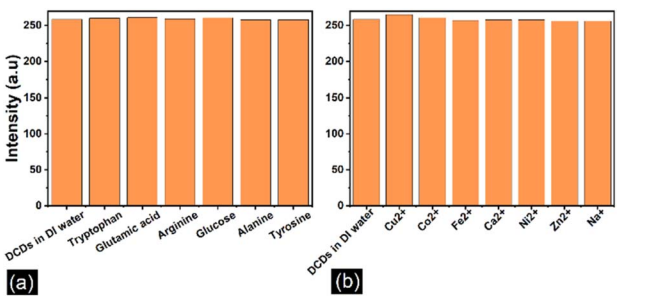

Fig. 10 (a) Anti-interference of the DCDs in the presence of different amino acids (1 mmol L^{-1}). (b) The changes in the fluorescence intensity of DCDs in the presence of various metal ions (1 mmol L^{-1}).

UV light for 1000 seconds. This remarkable photostability demonstrates that the DCD probe has a significant resistance to photobleaching and photo-induced breakage.

3. Experimental details

3.1 Materials and methods

Methanol, CA, DMF, tris buffer, formamide, PEG400, acetone, DMSO, and glycerol were purchased from Sisco Research Laboratories, India. DI water was collected from a milli-pore water purification system (≥18 MW, Milli-Q, Millipore). Technical grade OA and bovine serum albumin (BSA) were obtained from Aldrich (Sigma-Aldrich, Singapore). Dulbecco's modified Eagle's medium (DMEM), fetal bovine serum (FBS) and phosphate buffered saline (PBS) were procured from Gibco (Thermo Fisher, Singapore), and LipidSpot 488 lipid droplet dye was purchased from Biotium (Atlantis Bioscience, Singapore).

UV-visible absorption and PL spectra were recorded using a Jasco V-570 spectrophotometer and Jasco FP-6600 spectrofluorometer. The morphology and size distribution of the DCDs were characterized through high-resolution transmission electron microscopy (HR-TEM) imaging utilizing a JEOL 3010 microscope. The statistical analysis of the samples was carried out using ImageJ software. XRD patterns were recorded on an Aeris Benchtop X-ray Diffractometer (PANalytical) with graphite-monochromatic Cu Kα radiation ($\lambda = 0.1518$ nm). The FTIR spectra were recorded with a Bruker VERTEX 70 spectrometer. The Raman spectra were recorded using a Horiba Jobin Yvon Model HR800 Raman spectrometer (632 nm). A Carl Zeiss LSM 800 CLSM was used for cellular fluorescence imaging.

3.2 Synthesis of DCDs

The DCDs were synthesized by the solvothermal method in which 3.5 g CA, 2 g tris buffer, and 5 mL PEG400 were dissolved in 20 mL of an aqueous formamide solution in a 1 : 1 ratio.[52] The solution was thoroughly mixed using a magnetic stirrer until the solution became transparent. The as-prepared solution was then transferred to a Teflon-lined autoclave (50 mL) and placed inside a hot air oven at 200 °C for 10 hours. Following the reaction, the solution was cooled to ambient temperature, and the resulting solution was filtered through a 0.22 μm syringe filtration membrane to remove larger particles. Subsequently, acetone was added to precipitate the DCDs, and the precipitate was collected by centrifuging at 10 000 rpm and then washed twice with ethanol. The synthesized DCDs were further purified by dialysis using a 3.5 kDa membrane for 24 hours against DI water. It was reported that CA and tris could be carbonized into blue CDs with a photoluminescence quantum yield (PLQY) of nearly 100%.[53] Adding formamide increased the content of graphitic nitrogen in the CDs and changed their emission from blue to red.[38] The synthesis process was optimized by varying the annealing time and temperature. The as-prepared DCDs were dissolved in DI water (1 mg mL^{-1}) and DMSO (1 mg mL^{-1}) as stock solutions for spectroscopic studies. Different micropolarity values in solution were obtained by mixing DI water and DMSO solutions, and the final concentration of DCDs was kept fixed at 10 μg mL^{-1}. The DCDs dissolved in DI water (5 μg mL^{-1}) were used for biological experiments. For anti-interference measurement of DCDs, appropriate amounts of NaCl, $ZnCl_2$, $NiCl_2$, $CaCl_2$, $FeCl_2$, $CoCl_2$, $CuCl_2 \cdot 2H_2O$, L-tyrosine, L-alanine, L-glutamic acid, L-arginine, L-tryptophan and glucose were weighed out and dissolved in DI water to obtain a final working concentration of 1 mmol L^{-1} of metal ions and amino acids.

3.3 Preparation of the OA/BSA complex

The OA was kept in a temperature bath at 37 °C until it was liquefied completely. The OA was then diluted to 150 mM in ethanol (50%) by adding 47 μL of OA (90%) to 953 μL of ethanol and mixing with a vortex mixer. The resulting mixture became a cloudy white suspension. The 150 mM OA was stored at 4 °C and warmed to 37 °C before use. The defatted BSA (100 mg mL^{-1}) was dissolved in DI water and maintained at −20 °C. The OA/BSA complex was freshly prepared on the day of the experiment. To prepare the OA/BSA complex, equal volumes of 150 mM OA and 100 mg mL^{-1} defatted BSA in DI water were mixed. The OA/BSA complex was thoroughly mixed and incubated at 37 °C for 1 hour. The OA/BSA complex was then diluted to a 1 : 150 ratio in a complete cell culture medium (CM) to obtain a final concentration of 150 μM OA. The cells were incubated with 150 μM OA for 16 hours in a humidified environment with a 5% CO_2 atmosphere at 37 °C. Cells treated with only the CM, without adding OA, served as the control for the experiment.

3.4 Cell culture and cytotoxicity studies

HeLa cells were grown in a CM containing 90% DMEM, 9% FBS, and 1% penicillin and streptomycin. The MTT assay was utilized to evaluate the cellular toxicity of the DCDs. HeLa cells were seeded in a 96-well plate at a concentration of 5000 cells/100 μL in each of the wells and incubated for 24 hours. After 24 hours, the medium was aspirated and washed twice with PBS. Then, 100 μL of modified CM containing varying amounts of DCDs (0, 1, 2, 5, 10, 25, 50, and 100 μg mL^{-1}) was added and incubated for another 24 hours. Then, the medium was removed, and 100 μL DMEM containing 5 mg mL^{-1} MTT (10% of the added culture medium) was added to each well. After 2 hours, the supernatant solution was extracted without disturbing the purple-coloured formazan salts that formed. 100 μL of DMSO was added to each well to dissolve them. The resulting mixture was shaken at room temperature for 45 seconds, and the optical density (OD) of each well was measured using a microplate reader set at a wavelength of 570 nm. The wells treated with 0% DCDs were used as controls. The following equation was used to estimate cell viability (%):

$$\text{Cell vaibility}(\%) = \frac{\text{OD}_{\text{treated}}}{\text{OD}_{\text{control}}} \times 100\%$$

where $OD_{treated}$ and $OD_{control}$ are the OD of the wells treated with DCDs and without DCDs, respectively.

3.5 Cell imaging and colocalization

The HeLa cells (5×10^4) were seeded in a 24-well plate containing a coverslip (0.17 mm) and incubated for 24 hours. After 24 hours, the culture medium was removed, and the modified medium with OA (150 μM) was added to the cells. The OA-treated cells were incubated for 16 hours to induce LDs.[54] Then, the medium with OA was aspirated and washed twice with PBS. DCDs in complete medium at a concentration of 5 μg mL^{-1} were added to the cells and incubated for another 6 hours. After washing twice with PBS, the cells were treated with 1X LipidSpot 488 dye in DMEM and incubated for 30 minutes. A confocal laser scanning microscope was used to image cellular fluorescence at different excitation wavelengths.

4. Conclusions

In this study, DCDs were synthesized through the solvothermal method, employing optimized conditions. The synthesized DCDs demonstrated excitation-independent emission and the obtained results illustrated dual-emission properties in the blue and red spectral regions under a single excitation wavelength. It is clear that DCDs are highly sensitive to polarity, and the ratio of fluorescent emission intensities at 645 nm and 450 nm demonstrated a linear relationship with the range of polarity change (Δf from 0.235 to 0.318). DCDs could be used to detect a very small micro-scale polarity change and serve as a ratiometric fluorescent nanoprobe for precise polarity sensing without any modification. The synthesized DCDs exhibited solvatochromism, superior photostability, good biocompatibility, and specific LD targeting and imaging ability. The selectivity study of DCDs against various metal ions and biologically relevant amino acids further validates its exceptional specificity for LDs. In conclusion, we have successfully developed a facilely synthesised polarity-sensitive ratiometric fluorescent sensor that holds great promise for applications in biomedical research associated with LDs.

Data availability

The data that support the findings of this work are available from the corresponding author [Jayeeta Bhattacharyya] on reasonable request.

Author contributions

Aminakutty Neerkattil: conceptualization, data curation, formal analysis, investigation, methodology, validation, visualization, writing – original draft, and writing – review & editing. M. M. Bijeesh: conceptualization, data curation, formal analysis, investigation, methodology, validation, visualization, writing – original draft, and writing – review & editing. K. K. Ghosh: conceptualization, formal analysis, investigation, methodology, validation, visualization, and writing – review & editing. Parasuraman Padmanabhan: conceptualization, formal analysis, methodology, supervision, validation, visualization, and writing – review & editing. Balázs Gulyás: conceptualization, funding acquisition, project administration, supervision, validation, visualization, and writing – review & editing. V M. Murukeshan: conceptualization, funding acquisition, project administration, supervision, validation, visualization, and writing – review & editing. Jayeeta Bhattacharyya: conceptualization, funding acquisition, project administration, supervision, validation, visualization, and writing – review & editing.

Conflicts of interest

The author(s) report no conflicts of interest in this work.

Acknowledgements

AN is grateful to NTU-India Connect for the research internship opportunity. AN and JB express their gratitude for the financial assistance provided by the TINGE research centre, which is part of the IoE scheme at IIT Madras. AN and JB also thank and acknowledge Prof. N Sujatha and Dr Maitrayee Trivedi from the Biophotonics Lab, Department of Applied Mechanics and Biomedical Engineering, IIT Madras, for their support and valuable insights. AN, BMM and MVM thank the research manpower and facilities provided through COLE-EDB funding at COLE, NTU. They also acknowledge the financial support received through the Ministry of Education, Singapore, under its Academic Research Fund Tier 1 (RG119/21). AN, BMM, KKG, BG, and PP are thankful for the support from the Cognitive Neuro Imaging Centre (CONIC) at NTU.

References

1 P. Lesani, A. H. M. Hadi, M. Khetarpaul, Z. Lu, E. J. New and H. Zreiqat, *Adv. Photonics Res.*, 2024, **5**, 2300245.
2 A. Zadoorian, X. Du and H. Yang, *Nat. Rev. Endocrinol.*, 2023, **19**, 443–459.
3 Y. Tatenaka, H. Kato, M. Ishiyama, K. Sasamoto, M. Shiga, H. Nishitoh and Y. Ueno, *Biochemistry*, 2019, **58**, 499–503.
4 Y. Hu, R. Q. Zhang, S. L. Liu and Z. G. Wang, *Biosens. Bioelectron.*, 2023, **240**, 115649.
5 M. Schuhmacher, A. T. Grasskamp, P. Barahtjan, N. Wagner, B. Lombardot, J. S. Schuhmacher, P. Sala, A. Lohmann, I. Henry, A. Shevchenko, Ü. Coskun, A. M. Walter and A. Nadler, *Proc. Natl. Acad. Sci. U. S. A.*, 2020, **117**, 7729–7738.
6 G. Onal, O. Kutlu, D. Gozuacik and S. Dokmeci Emre, *Lipids Health Dis.*, 2017, **16**, 128.
7 P. Dalhaimer, *Cells*, 2019, **8**, 974.
8 J. Yin, M. Peng and W. Lin, *Sens. Actuators, B*, 2019, **288**, 251–258.
9 J. Hu, Y. Sun, X. Geng, J. Wang, Y. Guo, L. Qu, K. Zhang and Z. Li, *Light: Sci. Appl.*, 2022, **11**, 185.
10 T. K. Fam, A. S. Klymchenko and M. Collot, *Materials*, 2018, **11**, 1768.
11 G. R. V. Hammond, M. M. C. Ricci, C. C. Weckerly and R. C. Wills, *Mol. Biol. Cell*, 2022, **33**, 2015.
12 Y. Zhao, W. Shi, X. Li and H. Ma, *Chem. Commun.*, 2022, **58**, 1495–1509.

13 J. Liu, R. Li and B. Yang, *ACS Cent. Sci.*, 2020, **6**, 2179–2195.
14 A. Babusenan, B. Pandey, S. C. Roy and J. Bhattacharyya, *Carbon*, 2020, **161**, 535–541.
15 R. V. Nair, P. Padmanabhan, B. Gulyás and M. V. Matham, *Plasmonics*, 2021, **16**, 863–872.
16 H. Ding, X. H. Li, X. B. Chen, J. S. Wei, X. B. Li and H. M. Xiong, *J. Appl. Phys.*, 2020, **127**, 231101.
17 Q. Zeng, H. Qi, T. Jing, J. Li, S. Shen, H. Zhao and Y. Gao, *ACS Photonics*, 2024, **11**, 5137.
18 M. Alafeef, I. Srivastava, T. Aditya and D. Pan, *Small*, 2024, **20**, 2303937.
19 Q. Mao, Y. Meng, Y. Feng, H. Li and T. Ma, *Inorg. Chem. Front.*, 2024, **11**, 713–734.
20 N. K. Tan, H. Chan, Z. Lu, H. Zreiqat, G. Lakhwani, P. Lesani and E. J. New, *ACS Appl. Mater. Interfaces*, 2024, **16**, 47303–47313.
21 M. X. Liu, N. Ding, S. Chen, Y. L. Yu and J. H. Wang, *Anal. Chem.*, 2021, **93**, 5284–5290.
22 D. Gao, A. Liu, Y. Zhang, Y. Zhu, D. Wei, J. Sun, H. Luo and H. Fan, *Chem. Eng. J.*, 2021, **415**, 128984.
23 D. Gao, Y. Zhang, Y. Zhu, N. Xin, D. Wei, J. Sun and H. Fan, *Carbon*, 2023, **202**, 265–275.
24 Y. Zhao, W. Shi, X. Li and H. Ma, *Chem. Commun.*, 2022, **58**, 1495–1509.
25 J. Ma, L. Sun, F. Gao, S. Zhang, Y. Zhang, Y. Wang, Y. Zhang and H. Ma, *Molecules*, 2023, **28**, 8134.
26 H. Zhu, J. Fan, H. Mu, T. Zhu, Z. Zhang, J. Du and X. Peng, *Sci. Rep.*, 2016, **6**, 1–10.
27 Q. Hu, H. Zhang, P. Ye, S. Ma, X. Zhu and Y. Bai, *Dyes Pigm.*, 2023, **208**, 110874.
28 B. Bin Chen, M. L. Liu, Y. T. Gao, S. Chang, R. C. Qian and D. W. Li, *Nano Res.*, 2022, **16**, 1064–1083.
29 R. C. Castro, R. N. M. J. Páscoa, M. L. M. F. S. Saraiva, J. L. M. Santos and D. S. M. Ribeiro, *Spectrochim. Acta, Part A*, 2022, **267**, 120592.
30 G. Huang, X. Luo, X. He, Y. Han, H. Zhao, W. Tang, T. Yue and Z. Li, *Dyes Pigm.*, 2021, **196**, 109803.
31 W. Song, W. Duan, Y. Liu, Z. Ye, Y. Chen, H. Chen, S. Qi, J. Wu, D. Liu, L. Xiao, C. Ren and X. Chen, *Anal. Chem.*, 2017, **89**, 13626–13633.
32 X. Mei, D. Wang, S. Wang, J. Li and C. Dong, *Anal. Bioanal. Chem.*, 2022, **414**, 7253–7263.
33 M. Zhang, R. Su, J. Zhong, L. Fei, W. Cai, Q. Guan, W. Li, N. Li, Y. Chen, L. Cai and Q. Xu, *Nano Res.*, 2019, **12**, 815–821.
34 H. Li, H. G. Ye, R. Cheng, J. Guo, Z. Bin Liang, G. Li, Q. Li, C. F. Wang and S. Chen, *J. Lumin.*, 2021, **236**, 118092.
35 K. Wang, X. Wang, X. Liu, E. Li, R. Zhao and S. Yang, *J. Mol. Struct.*, 2022, **1263**, 133167.
36 L. Li, L. Shi, J. Jia, O. Eltayeb, W. Lu, Y. Tang, C. Dong and S. Shuang, *ACS Appl. Mater. Interfaces*, 2020, **12**, 18250–18257.
37 Y. Hu, Z. Yang, X. Lu, J. Guo, R. Cheng, L. Zhu, C. F. Wang and S. Chen, *Nanoscale*, 2020, **12**, 5494–5500.
38 Y. Zhang, H. Song, L. Wang, J. Yu, B. Wang, Y. Hu, S. Q. Zang, B. Yang and S. Lu, *Angew Chem. Int. Ed. Engl.*, 2021, **60**, 25514–25521.
39 W. U. Khan, D. Wang and Y. Wang, *Inorg. Chem.*, 2018, **57**, 15229–15239.
40 A. Oya and S. Otani, *Carbon*, 1979, **17**, 131–137.
41 S. Wu, W. Li, Y. Sun, X. Zhang, J. Zhuang, H. Hu, B. Lei, C. Hu and Y. Liu, *J. Colloid Interface Sci.*, 2019, **555**, 607–614.
42 Q. Zhang, R. Wang, B. Feng, X. Zhong and K. (Ken) Ostrikov, *Nat. Commun.*, 2021, **12**, 1–13.
43 B. Su, D. Gao, N. Xin, K. Wu, M. Yang, S. Jiang, Y. Zhang, J. Ding, C. Wu, J. Sun, D. Wei, H. Fan and Z. Guo, *Regener. Biomater.*, 2024, **11**, rbad109.
44 C. She, Z. Wang, J. Zeng and F.-G. Wu, *Carbon*, 2022, **191**, 636–645.
45 L. Pan, S. Sun, L. Zhang, K. Jiang and H. Lin, *Nanoscale*, 2016, **8**, 17350–17356.
46 B. Zhang, B. Wang, E. V. Ushakova, B. He, G. Xing, Z. Tang, A. L. Rogach and S. Qu, *Small*, 2023, **19**, 2204158.
47 A. Sciortino, E. Marino, B. Van Dam, P. Schall, M. Cannas and F. Messina, *J. Phys. Chem. Lett.*, 2016, **7**, 3419–3423.
48 F. Liu, M. H. Jang, H. D. Ha, J. H. Kim, Y. H. Cho and T. S. Seo, *Adv. Mater.*, 2013, **25**, 3657–3662.
49 Y. Zhao, L. Yu, Y. Deng, K. Peng, Y. Yu and X. Zeng, *Ceram. Int.*, 2023, **49**, 16647–16651.
50 Y. Byun, C. W. Jung, J. H. Kim and W. Kwon, *Dyes Pigm.*, 2023, **208**, 110895.
51 Y. Wang, G. Wang, K. Wang, Z. Wang, Y. Guo and H. Zhang, *Sens. Actuators, B*, 2018, **261**, 210–217.
52 Y. Zhang, H. Song, L. Wang, J. Yu, B. Wang, Y. Hu, S. Zang, B. Yang and S. Lu, *Angew. Chem., Int. Ed.*, 2021, **60**, 25514–25521.
53 Y. Zhang, X. Liu, Y. Fan, X. Guo, L. Zhou, Y. Lv and J. Lin, *Nanoscale*, 2016, **8**, 15281–15287.
54 G. G. Takir, Y. Ohsaki, K. Morotomi-Yano, K. ichi Yano and H. Saitoh, *Biochem. Biophys. Res. Commun.*, 2018, **504**, 485–490.